energies

MDPI

Article

Two-Dimensional URANS Numerical Investigation of Critical Parameters on a Pitch Oscillating VAWT Airfoil under Dynamic Stall

Tariq Ullah [1,*], Krzysztof Sobczak [1], Grzegorz Liśkiewicz [1] and Amjid Khan [2]

[1] Faculty of Mechanical Engineering, Institute of Turbomachinery, Lodz University of Technology, 90-924 Lodz, Poland; krzysztof.sobczak@p.lodz.pl (K.S.); grzegorz.liskiewicz@p.lodz.pl (G.L.)
[2] School of Mechanical and Aerospace Engineering, Oklahoma State University, Stillwater, OK 74078, USA; amjid.khan@okstate.edu
* Correspondence: tariq.ullah@dokt.p.lodz.pl

Abstract: In this paper, a thorough 2D unsteady computational fluid dynamic analysis was performed on a pitching airfoil to properly comprehend the dynamic stall and aerodynamic forces. The computational software ANSYS Fluent was used to solve the unsteady Reynolds-averaged Navier–Stokes equations. Low Reynolds number flows were modeled using the k-ω shear stress transport turbulence model. Aerodynamic forces, fluid flow structures, and flow separation delay angles were explored as a function of the Reynolds number, reduced frequency, oscillation amplitude, and mean angle of attack. The maximum aerodynamic forces, including lift, drag, and the onset of the dynamic stall, were all influenced by these variables. The critical parameters that influenced the optimum aerodynamic forces and ended up causing dynamic stall delay were oscillation amplitude and mean angle of attack. The stall angle was raised by 9° and 6°, respectively, and a large increment in the lift coefficient was also noted in both cases. Additionally, for the highest Reynolds number, a considerable rise in the maximum lift coefficient of 20% and a 28% drop in drag coefficient were observed, with a 1.5° delay in the stall angle. Furthermore, a significant increase of 33% in the lift force was seen with a rise of 4.5° in the stall angle in the case of reduced frequency.

Keywords: pitch oscillating airfoil; dynamic stall; unsteady aerodynamics; computational fluid dynamics

Citation: Ullah, T.; Sobczak, K.; Liśkiewicz, G.; Khan, A. Two-Dimensional URANS Numerical Investigation of Critical Parameters on a Pitch Oscillating VAWT Airfoil under Dynamic Stall. *Energies* **2022**, *15*, 5625. https://doi.org/10.3390/en15155625

Academic Editors: Rohit Dhariwal and Shreyas Bidadi

Received: 7 June 2022
Accepted: 27 July 2022
Published: 3 August 2022

1. Introduction

A decade later, the global energy demand will increase by more than two-thirds of what it is now. The elevated use of fossil energy has major negative implications for global warming [1]. Renewable energy sources are rapidly gaining the attention of energy experts, business practitioners, and government policymakers to minimize the dependence on fossil fuels. Additionally, renewable energy resources, including biomass, wind, solar, and geothermal, are increasingly used, becoming more economically productive, and are considered the most efficient way to address global warming issues [2,3]. Among these energy technologies, wind is a mature, sustainable, and viable clean energy source. It has emerged as the preferred energy source for both developed and developing countries aiming to expand energy supplies, minimize CO_2 emissions, grow new businesses, and create new job opportunities [4]. The overall wind power generation capacity was 800 GW at the end of 2021, according to the most recent Global Wind Survey [5]. However, wind energy, like all energy sources, has the potential to harm the environment by reducing, fragmenting, or degrading wildlife habitats, fish, and plants. Additionally, the rotating turbine blades might endanger flying fauna, such as birds and bats. The energy sector, mainly in developing countries and ecologically sensitive areas, is concerned about a profound ignorance of these environmental consequences [6,7]. Commonly, two kinds of

wind turbines, horizontal axis wind turbines (HAWTs) and vertical axis wind turbines (VAWTs), are used to capture and turn the kinetic energy of wind into electricity [8]. The high cost of energy of current HAWT installations, particularly with their expensive foundations, has hindered wind power expansion [9]. Considering the Darrieus VAWTs simple design, its aerodynamics are complicated and face various modeling challenges. The angle of attack (AOA) of the airfoil varies continuously as the turbine rotates, resulting in varying aerodynamic forces [10]. Because of the continuous variations in AOA, a VAWT airfoil suffers DS at low tip-speed ratios (TSRs), which has a major impact on the turbine output [11].

1.1. Overview of Dynamic Stall

The dynamic stall is characterized as a delay in flow separation around the wings and airfoil surfaces caused by variations in AOA during a transient motion [12]. Airfoils experiencing a pitching movement exhibit a stall that is different from the static stall observed in conditions of constant AOA. DS occurs when the stall angle and aerodynamic forces are significantly greater than their static counterparts [13]. The aerodynamic loads and moments exhibit a hysteresis that is not present in stationary airfoils. In the case of rotary machines, including wind turbines, compressors, and helicopter wings, the DS phenomenon can be significant [14]. As the AOA rises, the flow near the airfoil leading edge (LE) tends to roll up, forming a leading-edge vortex (LEV), which contributes suction to the airfoil upper portion [15]. The additional suction improves the lift force and delays flow separation to some angles of attack As the LEV extends downwards, it influences the thickness of the boundary layer [16]. Meanwhile, a trailing-edge vortex (TEV) develops. While being directed downstream, the LEV interacts with the TEV, which is then thrown into the wake [17]. During the downward pitching movement, this process is repeated, with the formation of a new LEV and TEV and their subsequent release into the wake, until the flow is reattached at low AOA. Significant variations, as well as large hysteresis in aerodynamic forces, lead to a substantial rise in stresses, making the rotors further vulnerable to dynamic loads. The most important flow features of DS are addressed by McCroskey et al. [13] and Lee et al. [16] in detail. Due to the variations in AOAs encountered by turbine rotors while operating, DS occurs repeatedly in VAWTs, particularly at low TSRs [18]. This affects turbine fatigue strength, noise emission, and power output. Additionally, small-scale H-type Darrieus VAWTs in urban area applications generally work at a Re of around 10^5. Because of the characteristics of the shear layer on an airfoil, the aerodynamic efficiency of the VAWT is very susceptible to a variety of parameters, particularly at Re ranges 10^4–10^6 [19]. The most important are the mean pitching angle (α_m), oscillation amplitude (α_p), and reduced frequency (k), as well as the airfoil shape, chord length, and operating conditions. It is widely acknowledged that the accuracy and efficiency of CFD analyses can be highly vulnerable to various numerical conditions under these parameters [20]. Numerous authors proposed different DS simulation models, with some comparing their findings to the well-known Leishman–Beddoes model [21]. Akay et al. [22], Wang et al. [23], and Buchner et al. [24] discussed and compared various types of turbulent flow models.

1.2. Parameters Influencing the Dynamic Stall

In wind turbines and hydro-power energy systems, various mechanisms may cause DS, including transversal blade vibration, pitching, yawing, fluid velocity changes, and even the turbine dynamic operation. Ferrari [25] examined the impact of pitching location on the aerodynamic characteristics of a NACA0012 airfoil. He illustrated that increasing the pitching location increases the lift coefficient. Nevertheless, this shift in the pitching location leads to an increase in the drag. An analysis of the effects of rotor blade thickness and camber on the performance of a 5 KW VAWT was performed by Danao et al. [26] using a 2D numerical simulation. The authors demonstrated that the thinner airfoil has a higher-pressure coefficient. Additionally, airfoils with small camber, such as the LS0421, typically perform better, whereas the NACA5522 with a 5% camber is inappropriate. Raeisi and

Alighanbari [27] demonstrated that TE curvature and airfoil thickness play an important role in premature flow separation of a pitching NACA23012 airfoil. E. Dumlupinar and V. Murthy [28] investigated the phenomena of the dynamic stall for airfoils and three-dimensional wings. Yi et al. [29] carried out numerical and experimental investigations on a pitch oscillating delta wing to analyze the lift characteristics and flow field. The findings demonstrate that, for higher reduced frequency, a stronger LEV with more circulation was created during upstroke pitching, which provided an extra lift boost at a high AOA. Coton et al. [30] studied and characterized the main features of the dynamic stalling process of three different wing planforms (a straight rectangular wing, a rectangular wing with swept tips, and a delta wing). The findings demonstrated that, in the static scenario, the shape of the wing planform considerably influences the mode of stalling. Additionally, the delta wing's vortex disintegration is gradually delayed to greater incidence with a raising pitch rate compared to the rectangular wings. Wang et al. [8] examined NACA0012 pitching airfoil at Re of 1.35×10^5. The findings showed major fluctuations in instantaneous forces. Except for cases with a high AOA, the CFD findings were in decent agreement with experimental data. Furthermore, the effects of turbulent flows were demonstrated by Refs [31,32]. LEV shedding has been described quantitatively by a group of researchers [33]. They discovered that fluid behavior is highly affected by a variety of variables, including airfoil shape, α_m, α_p, k, and, most significantly, Re. Akbari et al. [34] examined the influences of transient parameters, including k, α_m, pitch axis position, and Re ($3 \times 10^3 \leq Re \leq 10^4$), on the NACA0012 airfoil. According to their findings, an increase in k induces a delay in flow separation, while changing the pitching location has a minor effect. Similarly, Amiralaei et al. [35] determined that the variables Re, k, and α_p would affect the extreme value of the lift and drag forces for the $555 \leq Re \leq 5000$ range, and it was discovered that k and αp had little effect on the lift coefficient. The transient aerodynamic forces on S809 airfoil under a nonlinear oscillatory motion for a different range of k, α_m, and α_p have been explored by Ref [36] at Re = 10^6. The data showed that the maximum lift coefficient (Cl_{max}) was reached at higher AOA by raising the value of k. Lu et al. [37] investigated NACA0012 airfoil at Re = 1.35×10^4 and found that k, α_p, and airfoil curvature affect the instantaneous Cl, thrust generation, and flow structure. The DS of an S809 airfoil was studied by Karbasian et al. [38] for different values of k. The findings revealed that increasing the value of k gradually improves the aerodynamic performance of the oscillating airfoil while also reducing the size of the vortices created around it. Hand et al. [39] performed a study on NACA0018 and indicated that the increase in Re causes a higher AOA to postpone DS.

1.3. Goals and Objectives

Although the above-mentioned researchers have been able to highlight the effects of transient parameters under DS, not all the limitations have been reported to investigate the parameters that have a great impact on Cl, Cd, and influence delay in DS. Therefore, a comprehensive dynamic stall study is conducted in the present article for several parameters, including Re, k, α_m, and α_p, which govern the aerodynamics of an airfoil subject to a pitching movement. The numerical data are validated against experimental data presented in the literature. A qualitative analysis is established, which involves a detailed evaluation of the above-mentioned parameters using an oscillating VAWT airfoil.

2. Methodology

The methodology used in the computational analysis of DS for a pitch oscillating airfoil is shown in Figure 1. ANSYS Fluent was used to run numerical simulations on an oscillating airfoil [40,41]. The simulation model was first validated using the available experimental information on a VR-7 airfoil [42,43]. Then, the investigations were carried out for the airfoil of the H-type Darrieus VAWT manufactured by Aeolos Wind Energy Ltd., which provided data about the airfoil chord length and geometric coordinates [44]. The

impact of Re, k, α_m, and α_p on a pitch oscillating airfoil of VAWT was studied by evaluating Cl and Cd vs. AOA hysteresis curves and analyzing the flow structures in detail.

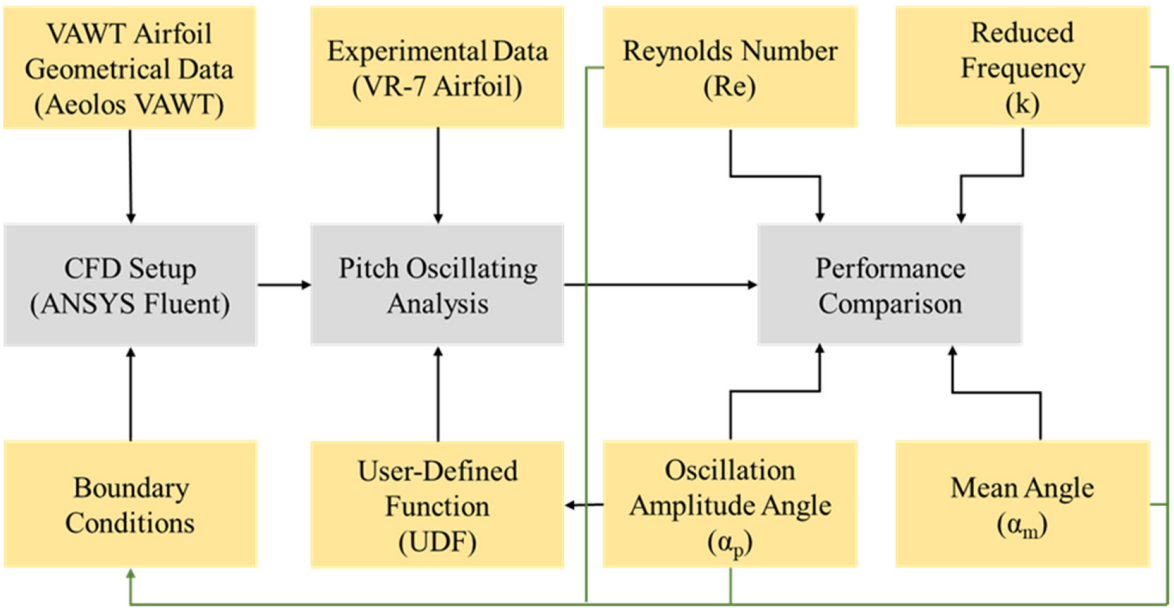

Figure 1. The methodology adopted for analysis of oscillating airfoil.

2.1. Computational Domain

Figure 2 depicts the computational domain. ANSYS Design Modeler was used to create the 2D model. The circular domain is divided into two zones: an external stationary zone and an internal oscillatory zone divided by an interface. The domain dimensions were selected based on the recommendations in Rezaeiha et al. [45]. The far-field zone is 15 times while the inner oscillating zone is 4 times the chord length (c = 450 mm) of the airfoil, respectively.

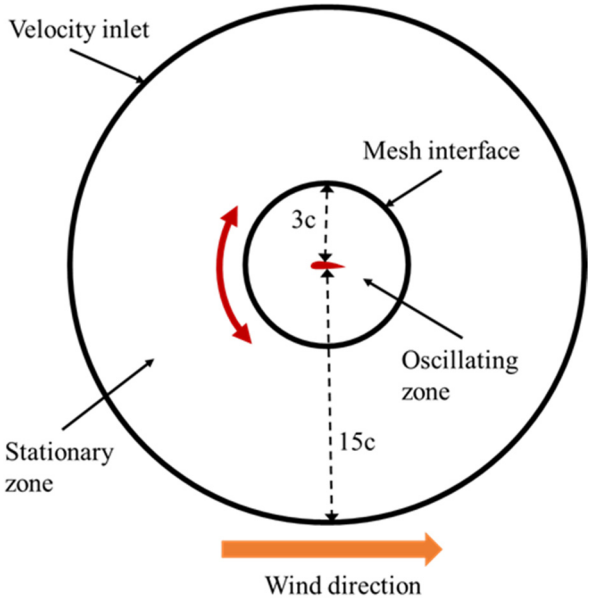

Figure 2. Computational domain specifications.

2.2. Grid Processing

A 2D unstructured grid is created using the ANSYS Mesh. Various mesh refinement methods are used to obtain accurate numerical results. Primarily, the mesh is refined in the internal zone. Additionally, to correctly reproduce the complexity of the flow fields around the airfoil, proper mesh sizing is required near the airfoil surface. The computational mesh is refined at the wall to guarantee that the first node meets the y+ $\leq$ 1 criterion. The first row of cells at the airfoil surfaces is 0.02 mm; 38 layers with a growth rate of 1.15 are applied, as shown in Figure 3.

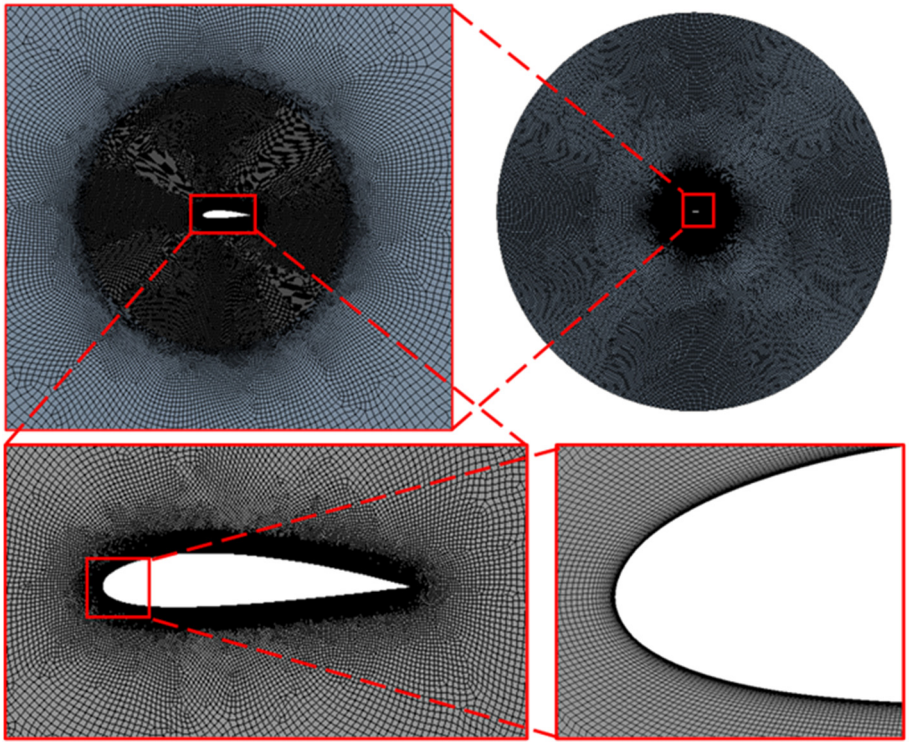

Figure 3. Computational mesh of 0.124 M elements with successive magnifications in the internal zone and around the airfoil.

Steady-state simulations of the flow around the airfoil at the angle of attack of 10° were carried out for the grid independence analysis. Table 1 shows the values of the lift and drag coefficient for the four considered meshes. The mesh of 0.124 M elements can be considered independent; thus, it is used in further studies.

Table 1. Mesh independence study results.

Mesh Size [Nodes]	81,574	104,360	123,910	151,060
Lift Coefficient [-]	1.1886	1.1868	1.1871	1.1871
Drag Coefficient [-]	0.2436	0.2431	0.2433	0.2433

2.3. Solver Setup

For all unsteady flow studies, the SST k-ω turbulence model is used, which is a widely accepted approach [46,47]. It is also frequently used in the VAWTs simulations [44,48]. Since VAWTs operate in the incompressible range, a pressure-based solver is used. The velocity inlet boundary condition with a wind velocity of 10 m/s and turbulence intensity of 1% is imposed on the boundary indicated in Figure 2. The no-slip, hydraulically smooth wall condition is applied at the airfoil surface. A user-defined function (UDF) of ANSYS Fluent is implemented to oscillate the internal zone for the pitch airfoil study [41]. The data transfer through the grid interface in the transient analysis is simulated using the

sliding mesh approach. A second-order upwind discretization of the mass, momentum, and turbulence model equations with the SIMPLE pressure-velocity coupling is utilized.

2.4. Specifications of Simulated Cases

The airfoil is oscillating around the axis at 25% of the airfoil chord length with the angle changing according to the formula:

$$\alpha = \alpha_m + \alpha_p \sin 2\pi f t \quad (1)$$

where the mean AOA, oscillation amplitude, and oscillation frequency are denoted by α_m, α_p, and f, respectively [17]. Reduced frequency k describes the unsteady aerodynamic behavior of an airfoil. It is used to illustrate the unsteadiness of the flow. When k = 0, the flow is in a steady state. For $k \geq 0$ and $k \leq 0.05$, the flow is in a quasi-state where the unsteadiness effects are small. For $k > 0.05$, the flow is in an unsteady state. It is defined in terms of the airfoil chord, angular frequency, and free stream velocity:

$$k = \frac{\omega * c}{2\, U_\infty} \quad (2)$$

2.5. Numerical Validation

Before being applied to the case study of the VAWT airfoil, the numerical method was set up and validated on a VR7 airfoil using the test case provided in Ref [43]. The simulations were performed at $Re = 2 \times 10^5$ with k = 0.10, $\alpha_m = 15°$, and $\alpha_p = 10°$ set to reproduce the experimental conditions. To restrict the interpolation inaccuracy at the sliding interface, the number of time steps per one oscillation cycle was kept in the range of 1200 to 1500 for all the simulated cases [20]. The time-step size $\Delta t = 1 \times 10^{-3}$ s was set for both VR7 and VAWT airfoil simulations.

Figure 4 shows the lift and drag coefficient curves during the upstroke and downstroke movement of the VR7 airfoil. The mean freestream velocity U_∞ was used to normalize the aerodynamic forces of lift L and drag D based on unit airfoil span, as follows:

$$[Cl,\ Cd] = \frac{[L, D]}{0.5 \rho U_\infty^2 c} \quad (3)$$

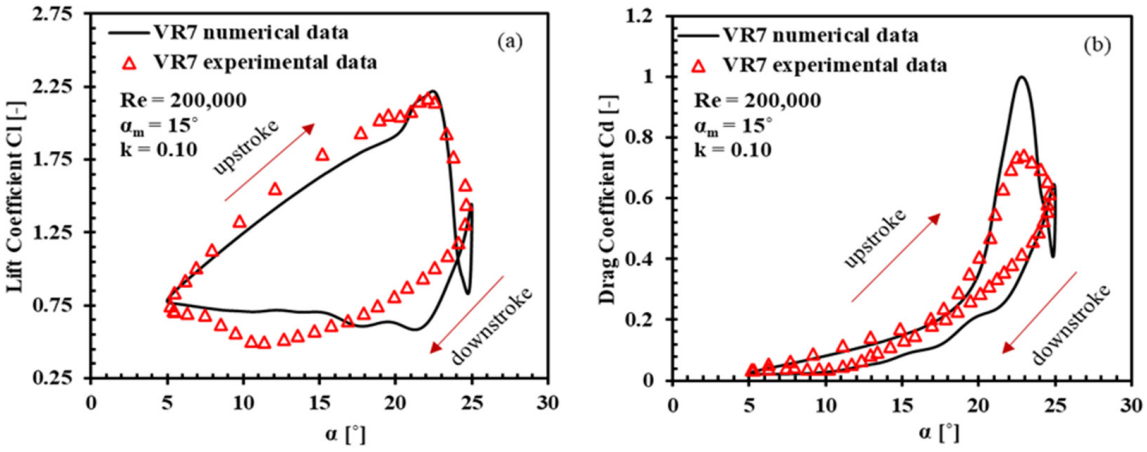

Figure 4. Validation of the pitch oscillating airfoil case utilizing VR7 airfoil experimental data to compare (**a**) coefficients of lift and (**b**) drag.

Regarding the Cl curve in Figure 4a, there is a good agreement between the simulation results and the test data. They coincide with each other well during the upstroke movement, followed by a stall at approximately $\alpha_{max} = 22°$ while maintaining a $Cl_{max} = 2.3$. During the downstroke movement, there is also decent agreement. Similarly, the Cd curve agrees for

most of the loop except at α_{max} (Figure 4b). This disagreement, as well as some discrepancy in the lift curves, can be related to the absence of surface roughness, lack of typical 2.5D effects present in the experimental tests, simplifications in the computational domain, and turbulence modeling for the numerically investigated VR7 case, which were also indicated by Ref [49,50]. Additionally, the skewness factor plays an important role in obtaining stable results, especially for the dynamic stall phenomena. In the current mesh, there were some areas close to the TE and LE where the average skewness was 0.12. Further, it was noted by Ref [20] that for an airfoil subjected to a pitching motion, the aerodynamic forces are much more sensitive to changes in the computational variables during the downstroke motion compared to the upstroke motion. Similar disagreement was reported by Ref [17], and according to their findings, mesh quality also plays an important role in obtaining stable results. Additionally, in their results, the simulated lift curve somewhat oscillates around the experimental results during the downstroke motion. They conclude that those small fluctuations were caused by reattachment and laminarization of the flow and had nothing to do with the mesh quality.

3. Results and Discussion

The impact of the Reynolds number reduced frequency, mean angle of attack, and oscillation amplitude on an oscillating airfoil of a VAWT is numerically studied by evaluating the Cl and Cd curves and analyzing the flow structures in detail.

3.1. Impact of the Reynolds Number

The effects of the Reynolds number changes between Re = 2–5 $\times$ 10^5 on Cl and Cd are studied in this section. The numerical simulations are run with k = 0.10, α_m = 15°, and α_p = 10° around the 25% of the airfoil chord length.

Figure 5a presents Cl vs. AOA, where the airfoil operating at Re = 5 $\times$ 10^5 exhibits the best performance. Higher values of Cl_{max} and α_{max} are obtained compared to lower Re cases. By raising the Reynolds number from Re = 2 $\times$ 10^5 to 5 $\times$ 10^5, the Cl_{max} rises 20% from 1.63 to 1.83, and the dynamic stall angle extends approximately from 21° to 22.5°, which delays the dynamic stall by 1.5°. Additionally, during the downstroke motion, the airfoil performance for higher Re shows better results. Although the results may differ somewhat in detail, there is no significant difference in the lift curves below 19°. The curves show a broad hysteresis loop, indicating that the stall is followed by extensive separations throughout the pitch-down portion of the cycle.

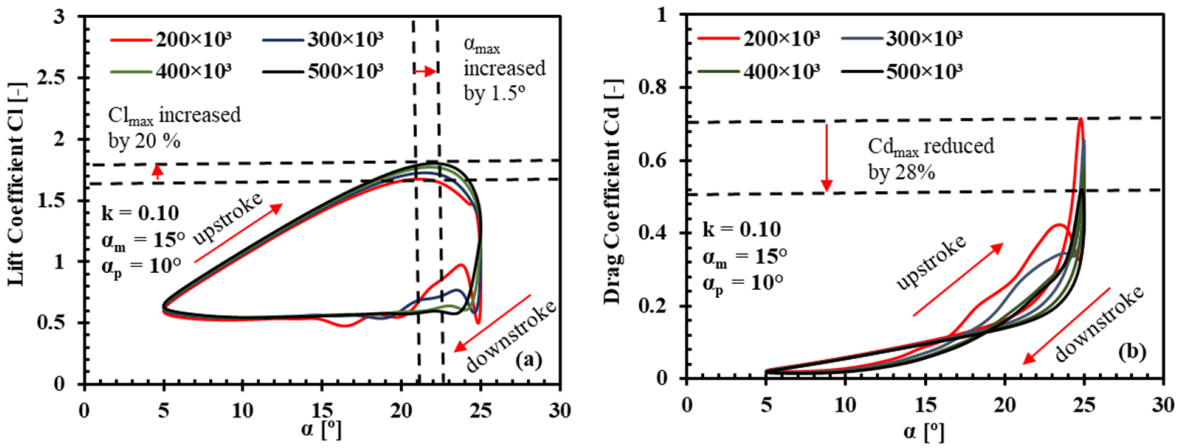

Figure 5. Comparison of hysteresis profiles for various Reynolds numbers for pitch oscillating airfoils: (**a**) Cl and (**b**) Cd at k = 0.10 and α_m = 15°.

Apart from Cl_{max} increasing with the increasing Reynolds number, Cd_{max} is also found to decrease, as shown in Figure 5b. The best performance is shown for Re = 5 $\times$ 10^5,

with a 28% decrease in Cd_{max} compared to Re = 2 × 10^5. In every case, the airfoil stall is indicated by the abrupt and substantial variations in the drag curves. At Re of 2 × 10^5 and 3 × 10^5, some local increase in the Cd is observed for the downstroke motion at $\alpha = 23°$. For this angle, some increase in the lift coefficient can also be noticed.

A better understanding of the pre-and post-stall phenomena requires an in-depth analysis of the fluid flow structures in combination with the aerodynamic loads. Figures 6 and 7 present the velocity and vorticity contours, respectively, for the selected AOA during the upstroke and downstroke motions of the pitching cycle. In both cases, the path lines are shown to visualize the flow pattern.

Starting with $\alpha = 16°$, during the upstroke motion (Figure 6), except for a slight separation at the airfoil suction side close to the TE, the flow remains attached to the airfoil for all Re values, with no indication of an LEV. A distinct TEV is formed when the airfoil oscillates higher to $\alpha = 20°$. For both AOAs, the flow separations are noticeably smaller for higher Reynolds numbers. The changes in the TEV size have an impact on the variation of the airfoil load. At $\alpha = 21.5°$, the lift reaches its maximum value for Re = 2 × 10^5. The first LEV extends along the suction side of the airfoil with the noticeable counter-rotating TEV at the TE (Figure 7). For Re = 5 × 10^5, both vortices are present, but they are significantly smaller, and the boundary layer remains attached for nearly half of the airfoil length. For this Reynolds number, the lift reaches its maximum at $\alpha = 23.5°$. One can notice that the separation sizes for this case are very similar to the case for Re = 2 × 10^5 at $\alpha = 21.5°$. At $\alpha = 25°$, for Re = 2 × 10^5, the airfoil is in the DS state, and the vortex shedding started with a secondary LEV appearing at the LE. Additionally, for Re = 5 × 10^5, the separation spreads over the whole suction side of the airfoil, resulting in an abrupt drop in the lift force.

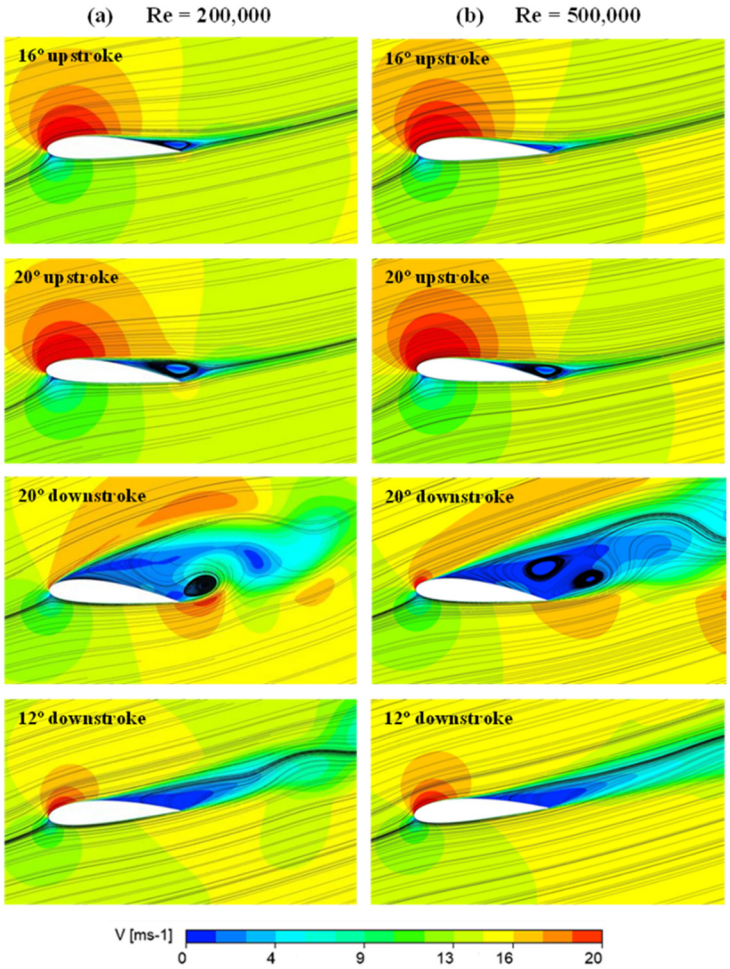

Figure 6. Velocity contours and streamlines at different α angles for (**a**) Re = 2 × 10^5 and (**b**) Re = 5 × 10^5.

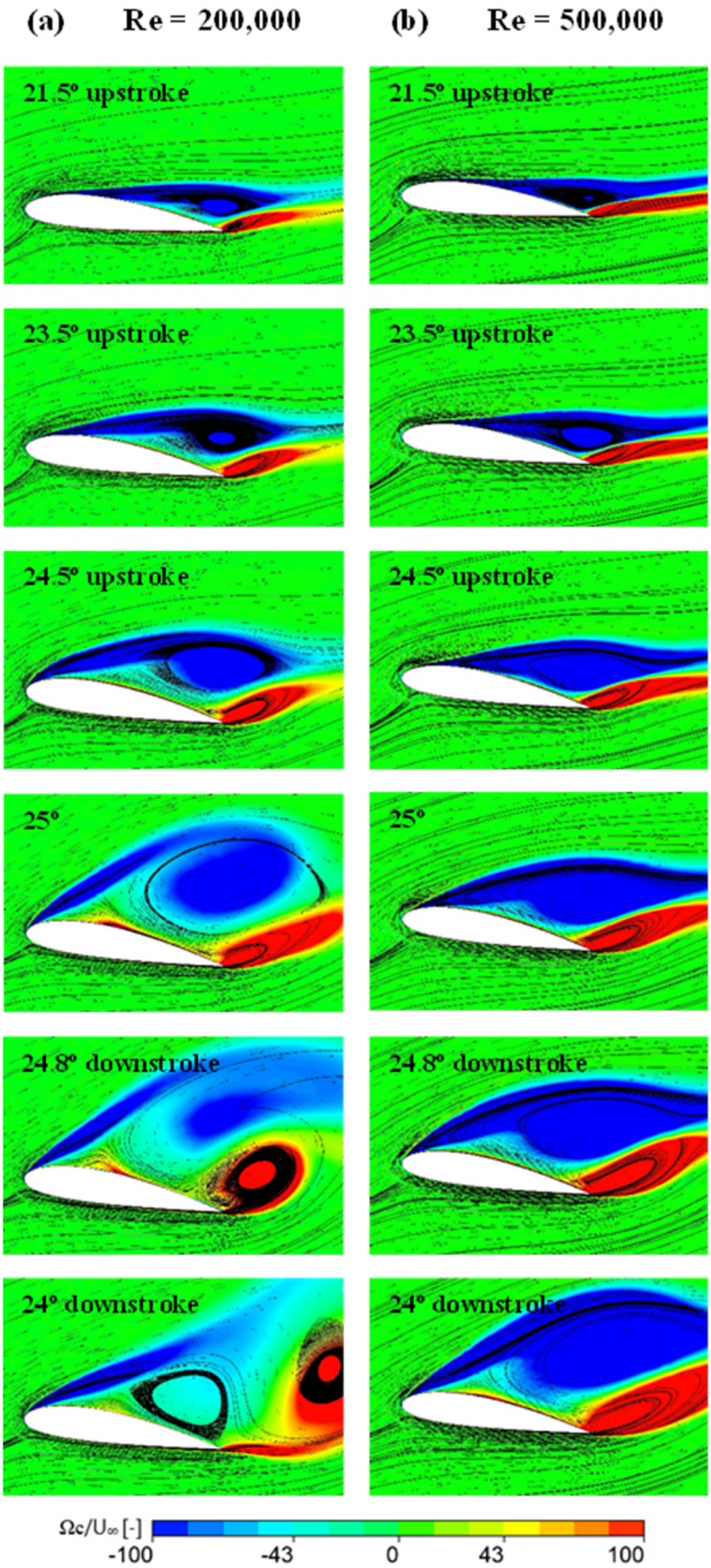

Figure 7. Vorticity contours at different α angles for (**a**) Re = 2×10^5 and (**b**) Re = 5×10^5.

As the airfoil for Re = 2 × 10^5 enters a downstroke movement, at $\alpha = 24.8°$, the first LEV detached into the wake, and the secondary LEV occupies most of the airfoil suction side. The creation of a secondary LEV can be ascribed to the local increase in Cl and Cd, for $\alpha = 25°$ to 23°. The TEV is also detached at $\alpha = 24°$ during the downstroke movement. Due to the delay in vortices shedding, the airfoil for higher Re has a lower Cl. However, because of large-scale separations and reattachments, the post-stall variations in the Cl and Cd are more significant for lower Re airfoils. The higher-Re number has a slightly stronger reattachment of the shear layer and flows stability from 16° to 12°, leading to a reduced hysteresis loop, as shown in Figures 5 and 6.

3.2. Impact of the Oscillation Amplitude

The influence of oscillation amplitude is investigated for $\alpha_p = 10°$, 15°, and 20°, at fixed values of k = 0.10, $\alpha_m = 15°$, and Re = 3 × 10^5.

Figure 8 presents the aerodynamic lift and drag coefficient loops. During the upstroke cycle, a huge increment is observed in lift and drag coefficients with increasing AOAs. The results also demonstrate that the Cl hysteresis curve widens with the rise in oscillation amplitude from 10° to 15°. For $\alpha_p = 10°$, at about 23°, the dynamic stall phenomenon occurs. However, the DS angle increases from 23° to 29° and 32°, respectively, for $\alpha_p = 15°$ and 20°. Additionally, a considerable rise in the value of Cl_{max} from 1.57 up to 2.12 and 2.51 is noted as the oscillation amplitude angle increases from $\alpha_p = 10°$ to $\alpha_p = 20°$ (see Figure 8a). Similarly, the value of the drag coefficient increases significantly with an increasing oscillation angle. The maximum drag coefficient Cd_{max} value increases from 0.67 up to 1.3 and 1.67 as the oscillation amplitude increases to 15° and 20°, respectively (see Figure 8b). Furthermore, during the downstroke cycle, oscillations in the aerodynamic curves are observed. These oscillations are due to the attachment and detachment of the flow from the airfoil upper section, and they are more prominent for lower oscillation amplitude angles.

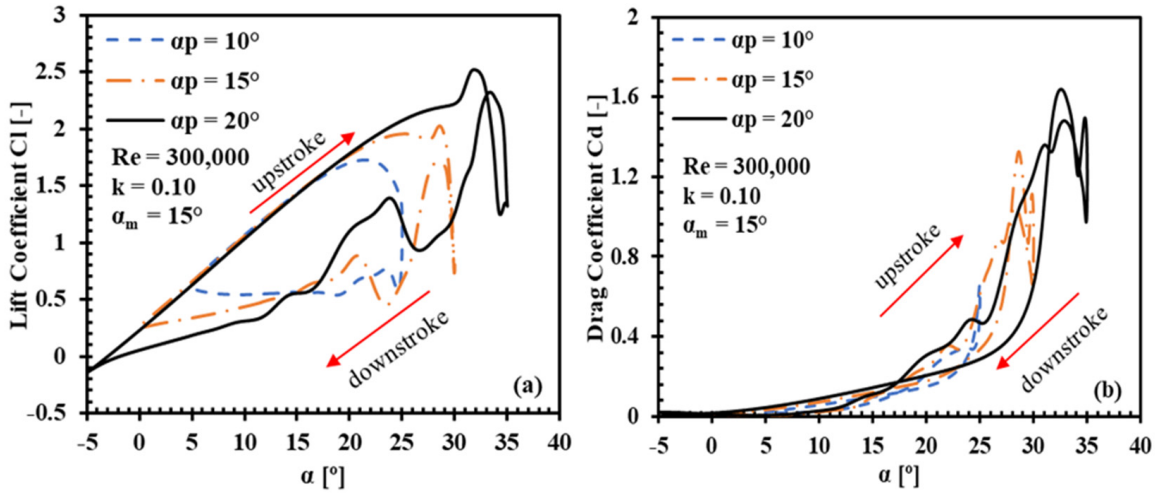

Figure 8. Aerodynamic coefficient curves: (**a**) Cl and (**b**) Cd for oscillation amplitudes $\alpha_p = 10°$, 15°, and 20°.

Upstroke and downstroke velocity contours with the streamlines presenting flow patterns are shown in Figure 9. In all cases, there is no noticeable flow detachment from the airfoil surface at lower AOAs. As the angle of attack increases, the flow starts to reverse and eventually detaches from the airfoil upper portion at a higher angle of attack. The dynamic stall phenomenon with LEV spreading over the airfoil suction side toward TE is observed at $\alpha = 24°$, 28°, and 32°, respectively, for all three cases.

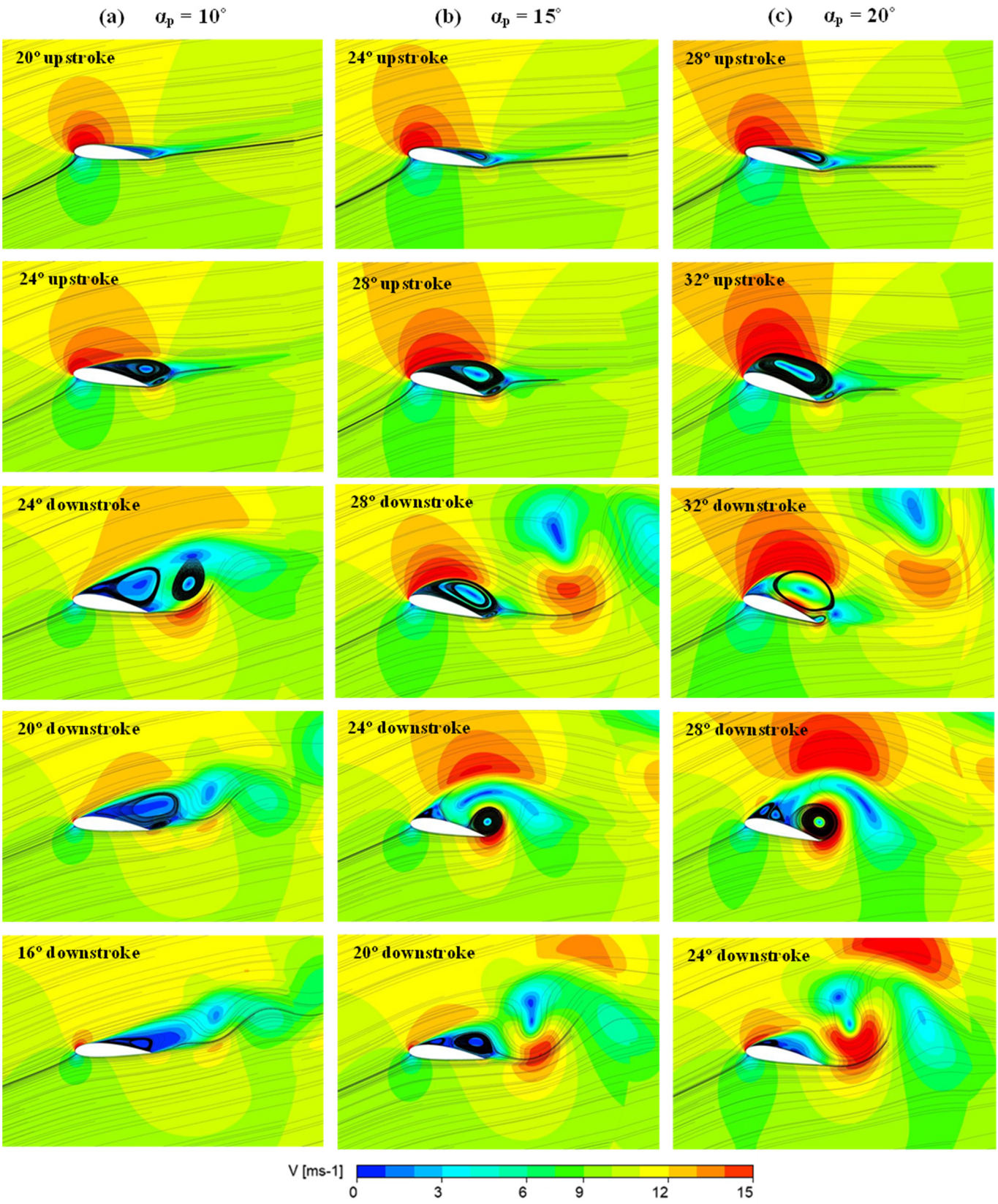

Figure 9. Velocity streamlines during upstroke and downstroke motions for oscillation amplitude angles of (**a**) 10°, (**b**) 15°, and (**c**) 20°.

For the oscillation amplitudes $\alpha_p = 10°$, during the downstroke motion at $\alpha = 24°$, a second LEV emerges after the first one is separated from the airfoil and moved into the wake (see Figure 9a). It causes the restoration of a small portion of Cl and Cd, from $\alpha = 25°$ to 23°. For higher oscillation amplitudes, much higher local increases in Cl and Cd are observed due to the development and shedding of LEVs and TEVs ($\alpha = 28°$ and 20° for $\alpha_p = 15°$; $\alpha = 32°$ and 24° for $\alpha_p = 20°$), as shown in Figure 9b,c). At lower AOA, a stronger reattachment of the boundary layer is observed, and the flow becomes more stable, leading to smoothly decreasing aerodynamic load curves. Overall, the higher oscillation amplitude airfoil behaves much better in terms of aerodynamic characteristics and fluid flow separation compared to the other two cases.

3.3. Impact of the Reduced Frequency

The effects of reduced oscillation frequency are investigated at fixed values of $\alpha_p = 10°$, $\alpha_m = 15°$, and $Re = 3 \times 10^5$ for a VAWT airfoil.

An increment occurred in both stall angle and hysteresis curves as the reduced frequency increases, as shown in Figure 10. The broadening of the hysteresis curves and the delay of flow separation are particularly visible for the lowest and the highest reduced frequencies, where stall angle is delayed up to 4.5°, and a massive increment of 33% occurs in Cl_{max}. A gradual decrease in the lift coefficient value for AOA beyond Cl_{max} is observed at low reduced frequencies (0.05 and 0.10) due to the flow separation from the TE of the airfoil. The widening of the drag hysteresis is also evident, especially at a higher reduced frequency. Compared to k = 0.05, the maximum drag coefficient at k = 0.20 drops due to the flow separation. Raising the reduced frequency postpones the drop in Cl gradient to greater AOA and boosts the pitching, which leads to increases in peak loads, including the lift and drag forces.

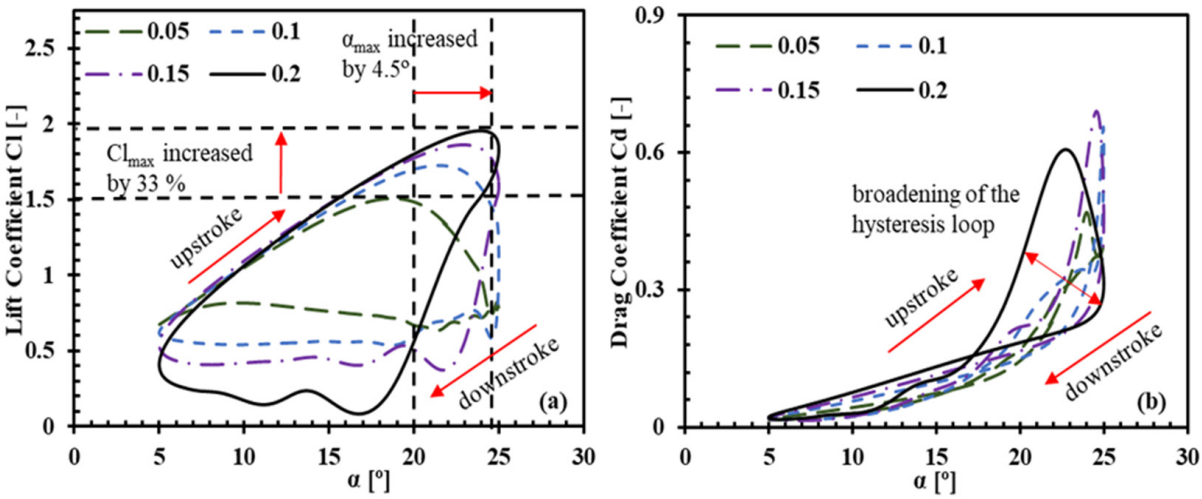

Figure 10. Aerodynamic coefficients of (**a**) lift and (**b**) drag for various reduced frequencies (k = 0.05, 0.10, 0.15, and 0.20).

The flow velocity distribution and streamlines for maximum and minimum reduced frequencies (0.05 and 0.20) are presented in Figure 11. At $\alpha = 12°$ during the upstroke movement, the flow remains fully attached to the majority of the airfoil upper surface in both cases, except for the small separation zone near the TE. When the airfoil moves further to $\alpha = 16°$, the separation zone becomes more visible in both cases. However, the TEV appears at the TE for lower reduced frequency, suggesting flow reversal, while for higher reduced frequency, the attached flow distribution is retained. The TEV increases in size as the airfoil oscillates to $\alpha = 20°$, and the boundary layer on the suction surface is about to separate at the LE for the k = 0.05 case. For the same AOA, a higher Cl, with only a small separation noted for the k = 0.20 case. With further increase in the upstroke angle, a

distinct LEV is formed, which interacts with the TEV and separates from the airfoil surface. An abrupt drop in Cl occurred, indicating a dynamic stall phenomenon for k = 0.05 as the airfoil moves to $\alpha = 24^{\circ}$. However, for k = 0.20, the origin of TEV is still away from the airfoil leading edge, with no indication of a dynamic stall phenomenon.

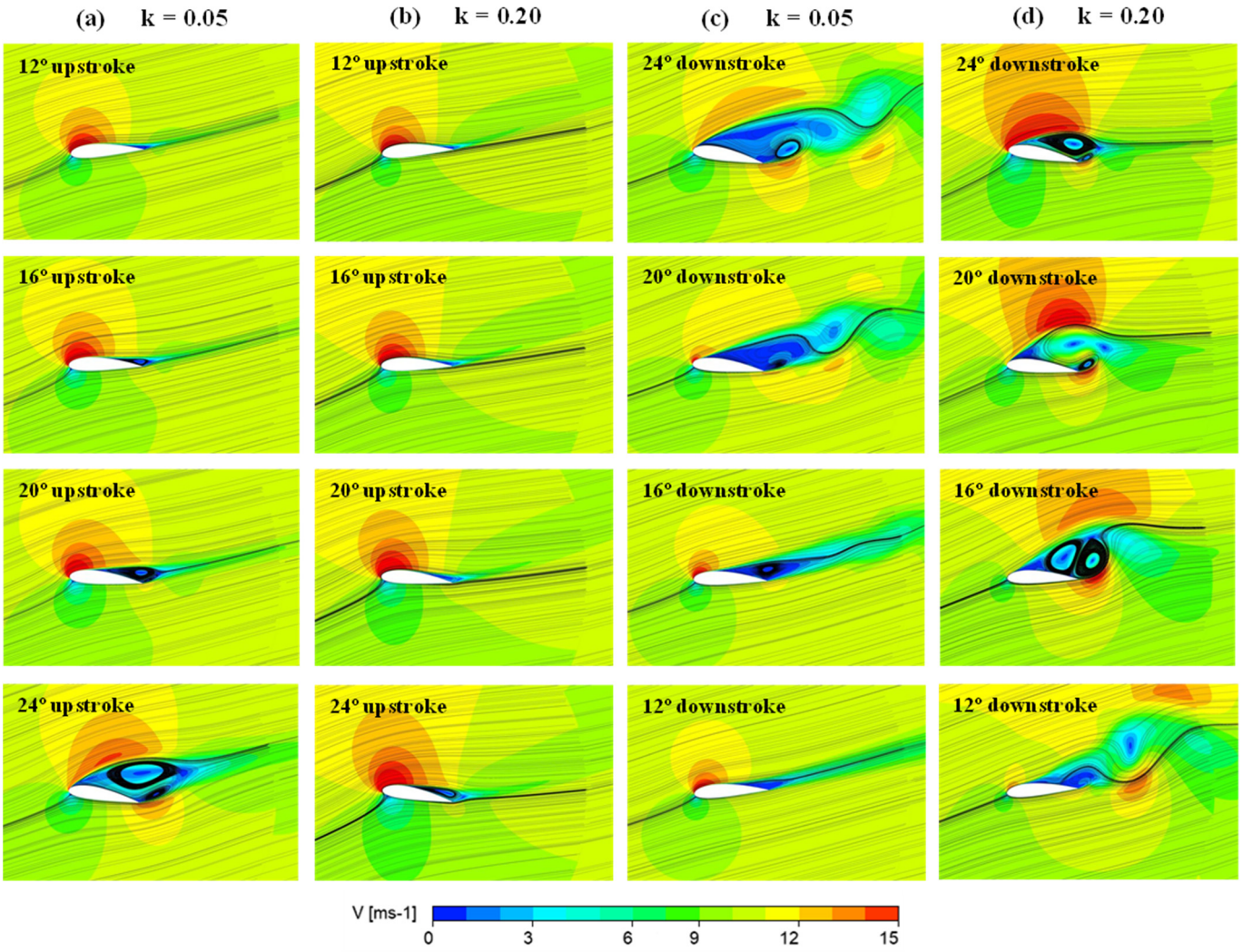

Figure 11. Velocity contours and streamlines at minimum k = 0.05 and maximum k = 0.20 during upstroke cycle (**a**,**b**) and downstroke cycle (**c**,**d**).

As the airfoil undergoes a downward movement to $\alpha = 24^{\circ}$, the flow is completely separated from the airfoil surface in the case of lower frequency (k = 0.05), while a noticeable LEV interacts with a TEV, leading to an increase and decrease in the drag and lift forces, respectively. Similarly, moving downward to $\alpha = 20^{\circ}$, significant flow separation with a further drop in the lift coefficient is noted in both cases. Furthermore, due to massive flow separations and reattachments, post-stall changes in the aerodynamic loads are noticeable in all cases (see Figure 10a,b). At $\alpha = 16^{\circ}$ downstroke for k = 0.20, there is a slight restoration in the Cl load due to the development of secondary vortices compared to k = 0.05. Additionally, for k = 0.05, the airfoil has a considerably better reattachment of the boundary layer and flows stability, resulting in reduced hysteresis curves below $\alpha = 12^{\circ}$, while for higher reduced frequency, Cl is further reduced due to the separation of secondary vortices. A much poorer airfoil performance is observed in the downward cycles for all cases. Improved results of the maximum left coefficient value (a huge increment of 33%) with delayed flow separation (delayed by 4.5°) are shown by the airfoil pitching with a maximum reduced frequency (k = 0.20) compared to the other three cases of medium to minimum

reduced frequency. Consequently, the improved results of the maximum left coefficient value with delayed flow separation are shown by the airfoil pitching with a maximum reduced frequency (k = 0.20) compared to the other three cases of medium to minimum reduced frequency.

3.4. Impact of the Mean Angle of Attack

In this section, the impact of the mean angle of oscillations over the range from 10° to 20° is numerically investigated. The Re value is set to Re = 3×10^5, k = 0.10, and $\alpha_p = 10°$.

As shown in Figure 12, raising the mean angle from $\alpha_m = 10°$ to $\alpha_m = 20°$ enlarges the lift and drag hysteresis and increases the amount of favorable pitching. During the upstroke section of the cycle, a common sequence of events occurs for all the mean angles evaluated. The flow is attached to the airfoil surface, and the aerodynamic loads' curves are parallel from lower to medium angles of attack. For $\alpha_m = 10°$, the flow separation starts early compared to the other two cases. A gradual reduction in the lift coefficient is noted without the dynamic stall event. However, the dynamic stall is observed for the higher mean angles of attack. The stall angle increases from 22° to 28° (6° increment) between the medium ($\alpha_m = 15°$) and the highest ($\alpha_m = 20°$) mean angles. Similarly, during the downstroke curves, fluctuations occur at higher angles of attack in the cases of 15° and 20° mean angles, as demonstrated in Figure 12a.

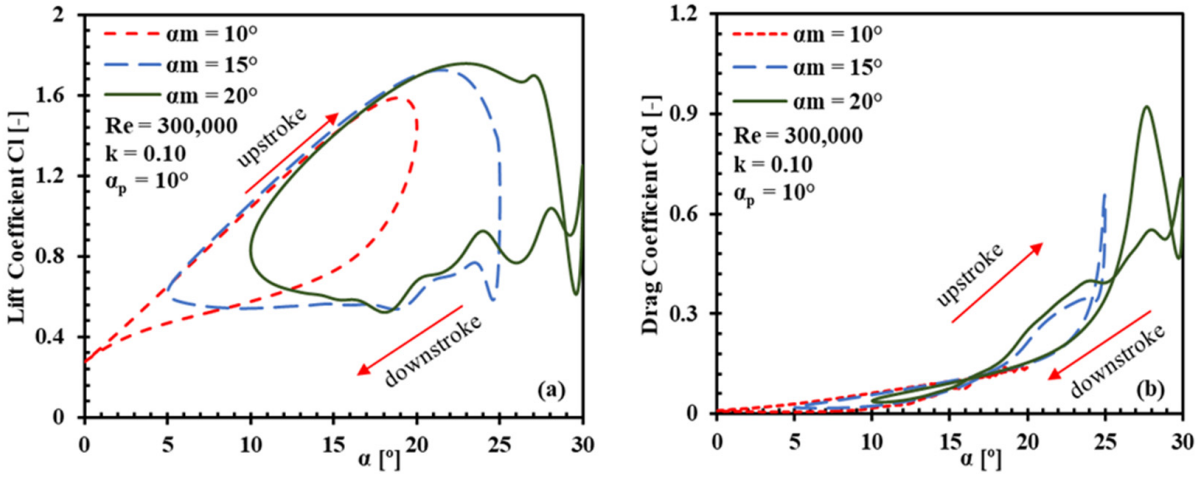

Figure 12. Aerodynamic coefficients of (**a**) lift and (**b**) drag for mean angles of 10°, 15°, and 20° during upstroke and downstroke motion.

Figure 13 depicts the velocity contours and streamlines during the upstroke and downstroke motion. For $\alpha_m = 10°$ (Figure 13a) during the upstroke motion, at $\alpha = 16°$, the flow stays attached to the airfoil suction side, with a small separation vortex appearing at the TE. It grows as the airfoil moves to $\alpha = 19°$; however, the dynamic stall phenomenon is not observed in this case. Meanwhile, during the downstroke motion, the fluid flow starts to separate at higher AOA, which results in a gradual reduction in the lift coefficient (see Figure 12a). From $\alpha = 19°$ to $\alpha = 16°$, the flow is trying to re-attach to the airfoil surface. When the airfoil moves down to lower angles of attack, a significant reduction is seen in the aerodynamic loads' hysteresis.

Further, during the upstroke motion at $\alpha = 19°$, the flow is mostly attached to the airfoil surface, but a small separation layer appears at the TE for $\alpha_m = 15°$ (Figure 13b). Similarly, the first LEVs grow at $\alpha = 24°$ upstroke, with the first TEVs appearing at the TE for $\alpha_m = 15°$ and $\alpha_m = 20°$ (see Figure 13b,c).

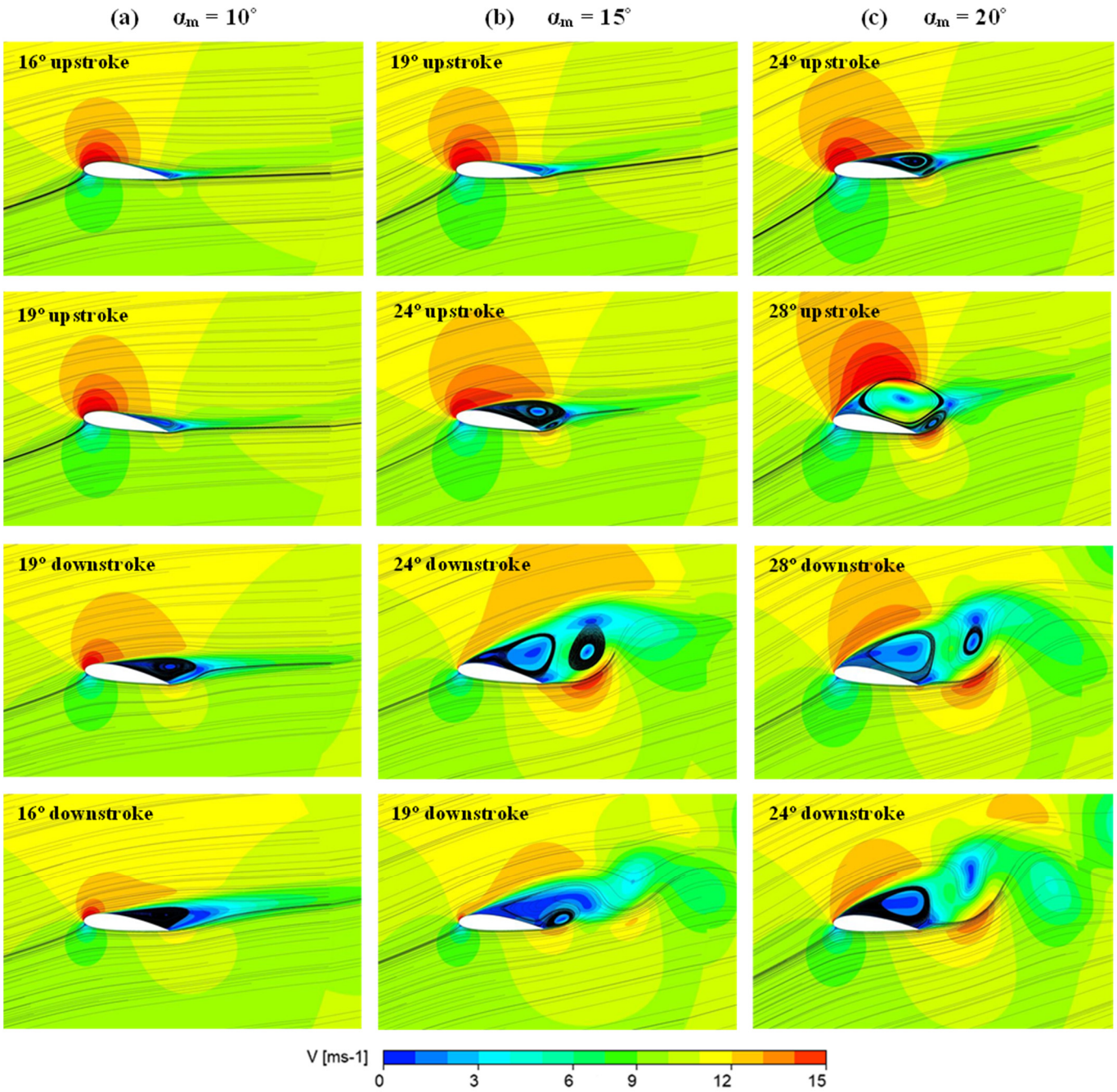

Figure 13. Velocity contours and streamlines during upstroke and downstroke motion for mean angles of (**a**) 10°, (**b**) 15°, and (**c**) 20°.

During the downstroke motion at $\alpha = 24^\circ$, the first LEV and TEV are separated from the airfoil surface, while a secondary LEV dominates the upper part of the airfoil for $\alpha_m = 15^\circ$. When the airfoil moves down to $\alpha = 19^\circ$, a secondary TEV appears, and the secondary LEV is thrown into the wake. Moreover, for $\alpha_m = 20^\circ$, as the airfoil progresses to $\alpha = 28^\circ$, the first LEV sheds into the wake; the dynamic stall phenomenon occurs, which results in a sharp fall in the lift coefficient (Figure 12a). When this airfoil goes through a downward movement at $\alpha = 28^\circ$, a second LEV develops and covers its upper side. The first TEV disperses in the wake, while the next one is about to develop. Additionally, a minor repair in Cl and Cd is noted from $\alpha = 26^\circ$ to 23° and $\alpha = 24^\circ$ to 22° for $\alpha_m = 20^\circ$ and $\alpha_m = 15^\circ$, respectively. The airfoils have considerably greater reattachment of the flow layer and flow steadiness at lower AOAs, with a reduction in hysteresis curves. A further

decrease in AOA during the downstroke motion causes a diminution of the separations. In conclusion, airfoil oscillating with a lower mean angle ($\alpha_m = 10^\circ$) shows better performance compared to the higher mean angles ($\alpha_m = 15^\circ$ and $\alpha_m = 20^\circ$) in terms of the aerodynamic loads, fluid flow separation, and dynamic stall.

4. Conclusions

The present study focused on the CFD modeling of the aerodynamic characteristics of a VAWT airfoil subjected to pitching motion under the dynamic stall. A 2D URANS method with the k-ω shear stress transport turbulence model was used to simulate the fluid flow around the airfoil. The impacts of critical unsteady parameters such as Reynolds number, reduced frequency, oscillation amplitude, and mean angle on the dynamic stall phenomenon, flow separation, and aerodynamic forces, were investigated. The main conclusions of the current research are as follows:

- Except for very high AOAs, when the flow is entirely separated, and the 3D impact is anticipated to be more evident, the SST k-ω turbulence model reasonably represents the experimental results. The turbulence model also showed the key dynamic stall features, including LEV-dominated flow structures, the aerodynamic load curves, and the secondary vortices in the downstroke motion.
- The influence of increasing the Reynolds number was investigated, where it was determined that the dynamic stall effects are delayed to higher angles of attack and, consequently, a considerable increment and decrement in the lift and drag coefficients were achieved, respectively.
- Additionally, the oscillation amplitude highly influences the dynamic performance of the airfoil. By raising the oscillation amplitude angle, a significant rise in Cl occurred, and a huge delay of 9° was observed in the dynamic stall angle. Also, a considerable increment was also noted in the Cd.
- Further, the reduced oscillation frequency impact on the dynamic stall phenomenon was also presented in detail. At the low angle of attacks, increasing the reduced frequency had little influence on the lift coefficient, while at a higher angle of attacks, the slope of the Cl decreased with decreasing reduced frequency. The dynamic stall was not observed at a maximum reduced frequency. Another finding was that the interaction between the LEV and TEV was stronger for the minimum reduced frequency compared to the maximum reduced frequency.
- Lastly, the numerical results of mean angles indicated that raising the mean angle enlarged the lift and drag hysteresis and increased the amount of favorable pitching. The dynamic stall for the lowest mean angle was not observed. Additionally, a delay in flow separation was noted with a substantial increment in the stall angle as the mean angle increased. Moreover, during downstroke cycles, for higher mean angles, some fluctuations in the curves occurred due to the attachment and detachment of the flow.

The capabilities of other more sophisticated CFD approaches, such as LES or DES, must be researched to gain a highly deep understanding of the complexities of the dynamic stall occurrence. In addition, extensive experimental tests and a three-dimensional numerical evaluation of the vertical axis wind turbine airfoil are needed.

Author Contributions: Conceptualization, T.U.; methodology, T.U.; software, T.U. and A.K.; validation, T.U.; formal analysis, K.S. and G.L.; investigation, T.U., G.L. and A.K.; data curation, T.U.; writing—original draft preparation, T.U.; writing—review and editing, T.U., K.S. and G.L.; visualization, T.U., K.S. and A.K.; supervision, K.S. and G.L. All authors have read and agreed to the published version of the manuscript.

Funding: This research received no external funding.

Institutional Review Board Statement: Not applicable.

Informed Consent Statement: Not applicable.

Data Availability Statement: Not applicable.

Acknowledgments: The authors would like to thank the Lodz University of Technology for offering the computing resources for this research.

Conflicts of Interest: The authors declare no conflict of interest.

Nomenclature

Variables

c	Chord length [m]
U_∞	Freestream velocity [m s^{-1}]
Cd	Drag coefficient [–]
Cl	Lift coefficient [–]
L	Lift [N]
D	Drag [N]
f	Frequency of oscillation [s^{-1}]
k	Reduced frequency [–]
v	Velocity [m s^{-1}]
Re	Reynolds number [–]
t	Time [s]
Δt	Time-step [s]
y+	Dimensionless near-wall distance [–]
ρ	Density [kg m^{-3}]
Ω	Vorticity [s^{-1}]
α_p	Amplitude angle of attack [°]
α_m	Mean angle of attack [°]
α	Instantaneous angle of attack [°]

Abbreviations

CFD	Computational Fluid Dynamics
DS	Dynamic Stall
DSV	Dynamic Stall Vortex
HAWT	Horizontal Axis Wind Turbine
VAWT	Vertical Axis Wind Turbine
URANS	Unsteady Reynolds-Averaged Navier–Stokes
LES	Large eddy simulation
DES	Detached eddy simulation
SST	Shear Stress Transport
LE	Leading Edge
LEV	Leading-Edge Vortex
TE	Trailing Edge
TEV	Trailing-Edge Vortex
AOA	Angle of attack

References

1. Martins, F.; Felgueiras, C.; Smitkova, M.; Caetano, N. Analysis of fossil fuel energy consumption and environmental impacts in european countries. *Energies* **2019**, *12*, 964. [CrossRef]
2. Mahmoudimehr, J.; Sorouri, A.; Feshalami, B.F. A novel map for deciding on the type of a hydro power plant. *Proc. Inst. Civ. Eng. Energy* **2016**, *169*, 161–178. [CrossRef]
3. Fridleifsson, I.B. Geothermal energy for the benefit of the people. *Renew. Sustain. Energy Rev.* **2001**, *5*, 299–312. [CrossRef]
4. Dai, K.; Bergot, A.; Liang, C.; Xiang, W.N.; Huang, Z. Environmental issues associated with wind energy—A review. *Renew. Energy* **2015**, *75*, 911–921. [CrossRef]
5. Lee, J.; Zhao, F. *Global Wind Report 2021*; Global Wind Energy Council: Brussels, Belgium, 2021; pp. 1–80. Available online: http://www.gwec.net/global-figures/wind-energy-global-status/ (accessed on 6 June 2022).
6. Leung, D.Y.C.; Yang, Y. Wind energy development and its environmental impact: A review. *Renew. Sustain. Energy Rev.* **2012**, *16*, 1031–1039. [CrossRef]
7. Saidur, R.; Rahim, N.A.; Islam, M.R.; Solangi, K.H. Environmental impact of wind energy. *Renew. Sustain. Energy Rev.* **2011**, *15*, 2423–2430. [CrossRef]
8. Wang, S.; Ingham, D.B.; Ma, L.; Pourkashanian, M.; Tao, Z. Numerical investigations on dynamic stall of low Reynolds number flow around oscillating airfoils. *Comput. Fluids* **2010**, *39*, 1529–1541. [CrossRef]
9. Bilgili, M.; Yasar, A.; Simsek, E. Offshore wind power development in Europe and its comparison with onshore counterpart. *Renew. Sustain. Energy Rev.* **2011**, *15*, 905–915. [CrossRef]
10. Halle, S.; Paraschivolu, I. Numerical Simulation of Dynamic Stall Around an Airfoil in Darrieus Motion. *J. Sol. Energy Eng.* **2016**, *121*, 69–76. Available online: http://solarenergyengineering.asmedigitalcollection.asme.org/ (accessed on 6 June 2022).
11. Amet, E.; Maître, T.; Pellone, C.; Achard, J.L. 2D numerical simulations of blade-vortex interaction in a darrieus turbine. *J. Fluids Eng. Trans. ASME* **2009**, *131*, 1111031–11110315. [CrossRef]
12. Carr, L. Dynamic stall progress in analysis and prediction. In Proceedings of the 12th Atmospheric Flight Mechanics Conference, Snowmass, CO, USA, 19–21 August 1985; Volume 25. [CrossRef]
13. McCroskey, W.J. The Phenomenon of Dynamic Stall. In *NASA Technical Memorandum 81264*; National Aeronautics and Space Administration Moffett Field Ca Ames Research Center: Mountain View, TX, USA, 1981; pp. 1–28.
14. Ullah, T.; Khan, A. Suppression of Dynamic Stall by Leading Edge Slat on a Darrieus Vertical Axis Wind Turbine. In Proceedings of the 2019 3rd International Conference on Energy Conservation and Efficiency (ICECE), Lahore, Pakistan, 23–24 October 2019; pp. 1–5. [CrossRef]
15. Leishman, J.G. Dynamic stall experiments on the NACA 23012 aerofoil. *Exp. Fluids* **1990**, *9*, 49–58. [CrossRef]
16. Lee, T.; Gerontakos, P. Investigation of flow over an oscillating airfoil. *J. Fluid Mech.* **2004**, *512*, 313–341. [CrossRef]

17. Gharali, K.; Johnson, D.A. Dynamic stall simulation of a pitching airfoil under unsteady freestream velocity. *J. Fluids Struct.* **2013**, *42*, 228–244. [CrossRef]
18. Rezaeiha, A.; Montazeri, H.; Blocken, B. Towards accurate CFD simulations of vertical axis wind turbines at different tip speed ratios and solidities: Guidelines for azimuthal increment, domain size and convergence. *Energy Convers. Manag.* **2018**, *156*, 301–316. [CrossRef]
19. Kim, D.H.; Chang, J.W. Low-Reynolds-number effect on the aerodynamic characteristics of a pitching NACA0012 airfoil. *Aerosp. Sci. Technol.* **2014**, *32*, 162–168. [CrossRef]
20. Geng, F.; Kalkman, I.; Suiker, A.S.J.; Blocken, B. Sensitivity analysis of airfoil aerodynamics during pitching motion at a Reynolds number of 1.35×10^5. *J. Wind Eng. Ind. Aerodyn.* **2018**, *183*, 315–332. [CrossRef]
21. Liu, P.; Yu, G.; Zhu, X.; Du, Z. Unsteady aerodynamic prediction for dynamic stall of wind turbine airfoils with the reduced order modeling. *Renew. Energy* **2014**, *69*, 402–409. [CrossRef]
22. Akay, B.; Ragni, D.; Simão Ferreira, C.J.; Van Bussel, G.J.W. Experimental Investigation of the root flow in a Horizontal Axis. *Wind Energy* **2013**, *17*, 1093–1109. [CrossRef]
23. Wang, S.; Ingham, D.B.; Ma, L.; Pourkashanian, M.; Tao, Z. Turbulence modeling of deep dynamic stall at relatively low Reynolds number. *J. Fluids Struct.* **2012**, *33*, 191–209. [CrossRef]
24. Buchner, A.J.; Lohry, M.W.; Martinelli, L.; Soria, J.; Smits, A.J. Dynamic stall in vertical axis wind turbines: Comparing experiments and computations. *J. Wind Eng. Ind. Aerodyn.* **2015**, *146*, 163–171. [CrossRef]
25. Ferrari, J.A. *Influence of Pitch Axis Location on the Flight Characteristics of a NACA 0012 Airfoil in Dynamic Stall*; Rensselaer Polytechnic Institute: Troy, NY, USA, 2012.
26. Danao, L.A.; Qin, N.; Howell, R. A numerical study of blade thickness and camber effects on vertical axis wind turbines. *Proc. Inst. Mech. Eng. Part A J. Power Energy* **2012**, *226*, 867–881. [CrossRef]
27. Raeisi, B.; Alighanbari, H. CFD analysis of oscillating blades for small horizontal axis wind turbines in dynamic stall condition. *Wind Eng.* **2014**, *38*, 499–522. [CrossRef]
28. Dumlupinar, E.; Murthy, V. Investigation of dynamic stall of airfoils and wings by CFD. In Proceedings of the 29th AIAA Applied Aerodynamics Conference, Honolulu, HI, USA, 27–30 June 2011; p. 3511.
29. Yi, Y.; Hu, T.; Liu, P.; Qu, Q.; Eitelberg, G.; Akkermans, R.A.D. Dynamic lift characteristics of nonslender delta wing in large-amplitude-pitching. *Aerosp. Sci. Technol.* **2020**, *105*, 105937. [CrossRef]
30. Coton, F.N.; Galbraith, R.A.M.D.; Green, R.B. The effect of wing planform shape on dynamic stall. *Aeronaut. J.* **2001**, *105*, 151–159. [CrossRef]
31. Choudhry, A.; Arjomandi, M.; Kelso, R. Horizontal axis wind turbine dynamic stall predictions based on wind speed and direction variability. *Proc. Inst. Mech. Eng. Part A J. Power Energy* **2013**, *227*, 338–351. [CrossRef]
32. Gharali, K.; Johnson, D.A. Numerical modeling of an S809 airfoil under dynamic stall, erosion and high reduced frequencies. *Appl. Energy* **2012**, *93*, 45–52. [CrossRef]
33. Lehmann, F.O. The mechanisms of lift enhancement in insect flight. *Naturwissenschaften* **2004**, *91*, 101–122. [CrossRef]
34. Akbari, M.H.; Price, S.J. Simulation of dynamic stall for a NACA 0012 airfoil using a vortex method. *J. Fluids Struct.* **2003**, *17*, 855–874. [CrossRef]
35. Amiralaei, M.R.; Alighanbari, H.; Hashemi, S.M. An investigation into the effects of unsteady parameters on the aerodynamics of a low Reynolds number pitching airfoil. *J. Fluids Struct.* **2010**, *26*, 979–993. [CrossRef]
36. Yu, G.H.; Zhu, X.C.; Du, Z.H. Numerical simulation of a wind turbine airfoil: Dynamic stall and comparison with experiments. *Proc. Inst. Mech. Eng. Part A J. Power Energy* **2010**, *224*, 657–677. [CrossRef]
37. Lu, K.; Xie, Y.H.; Zhang, D. Numerical study of large amplitude, nonsinusoidal motion and camber effects on pitching airfoil propulsion. *J. Fluids Struct.* **2013**, *36*, 184–194. [CrossRef]
38. Karbasian, H.R.; Moshizi, S.A.; Maghrebi, M.J. Dynamic stall analysis of S809 pitching airfoil in unsteady free stream velocity. *J. Mech.* **2016**, *32*, 227–235. [CrossRef]
39. Hand, B.; Kelly, G.; Cashman, A. Numerical simulation of a vertical axis wind turbine airfoil experiencing dynamic stall at high Reynolds numbers. *Comput. Fluids* **2017**, *149*, 12–30. [CrossRef]
40. ANSYS Inc. *ANSYS FLUENT 12.0 UDF Manual*; ANSYS Inc.: Canonsburg, PA, USA, 2009; Volume 15317, pp. 724–746.
41. ANSYS Inc. *ANSYS Fluent User's Guide Releasde 15.0*; ANSYS Inc.: Canonsburg, PA, USA, 2013; Volume 15317, pp. 724–746.
42. Ullah, T.; Javed, A. Numerical Investigation of VR-7 Airfoil Dynamic Stall Under Steady and Transient Conditions. In Proceedings of the 2nd Pak-Turk International Conference on Emerging Technologies in the field of Sciences and Engineering, Topi, Pakistan, 11–12 March 2019.
43. Mcalister, K.W.; Tung, C.; Aeronautics, N. *Suppression of Dynamic Stall with a Leading-Edge Slat on a VR-7 Airfoil*; National Aeronautics and Space Administration, Ames Research Center: Mountain View, CA, USA, 1993.
44. Ullah, T.; Javed, A.; Abdullah, A.; Ali, M.; Uddin, E. Computational evaluation of an optimum leading-edge slat deflection angle for dynamic stall control in a novel urban-scale vertical axis wind turbine for low wind speed operation. *Sustain. Energy Technol. Assess.* **2020**, *40*, 100748. [CrossRef]
45. Rezaeiha, A.; Kalkman, I.; Blocken, B. CFD simulation of a vertical axis wind turbine operating at a moderate tip speed ratio: Guidelines for minimum domain size and azimuthal increment. *Renew. Energy* **2017**, *107*, 373–385. [CrossRef]

46. Orlandi, A.; Collu, M.; Zanforlin, S.; Shires, A. 3D URANS analysis of a vertical axis wind turbine in skewed flows. *J. Wind Eng. Ind. Aerodyn.* **2015**, *147*, 77–84. [CrossRef]
47. Jiménez, J. The numerical computation of turbulence. In *Lecture Notes on Turbulence and Coherent Structures in Fluids, Plasmas and Nonlinear Media*; World Scientific: Singapore, 2006; pp. 281–307. [CrossRef]
48. Sobczak, K. Numerical investigations of an influence of the aspect ratio on the Savonius rotor performance. *J. Phys. Conf. Ser.* **2018**, *1101*, 012034. [CrossRef]
49. Karbasian, H.R.; Kim, K.C. Numerical investigations on flow structure and behavior of vortices in the dynamic stall of an oscillating pitching hydrofoil. *Ocean Eng.* **2016**, *127*, 200–211. [CrossRef]
50. Martinat, G.; Braza, M.; Hoarau, Y.; Harran, G. Turbulence modelling of the flow past a pitching NACA0012 airfoil at 105 and 106 Reynolds numbers. *J. Fluids Struct.* **2008**, *24*, 1294–1303. [CrossRef]